Theses and Dissertations   1. Thesis and Dissertation Collection, all items

2015-12

Characterization of piezoelectric energy harvesting MEMS

Johnson, Ryan D.

Monterey, California: Naval Postgraduate School

http://hdl.handle.net/10945/47971

NAVAL POSTGRADUATE SCHOOL

MONTEREY, CALIFORNIA

THESIS

CHARACTERIZATION OF PIEZOELECTRIC ENERGY HARVESTING MEMS

by

Ryan D. Johnson

December 2015

Thesis Advisor:	Dragoslav Grbovic
Co-Advisor:	Fabio Alves

Approved for public release; distribution is unlimited

THIS PAGE INTENTIONALLY LEFT BLANK

REPORT DOCUMENTATION PAGE		*Form Approved OMB No. 0704–0188*

Public reporting burden for this collection of information is estimated to average 1 hour per response, including the time for reviewing instruction, searching existing data sources, gathering and maintaining the data needed, and completing and reviewing the collection of information. Send comments regarding this burden estimate or any other aspect of this collection of information, including suggestions for reducing this burden, to Washington headquarters Services, Directorate for Information Operations and Reports, 1215 Jefferson Davis Highway, Suite 1204, Arlington, VA 22202-4302, and to the Office of Management and Budget, Paperwork Reduction Project (0704-0188) Washington, DC 20503.

1. AGENCY USE ONLY (*Leave blank*)	2. REPORT DATE December 2015	3. REPORT TYPE AND DATES COVERED Master's thesis	
4. TITLE AND SUBTITLE CHARACTERIZATION OF PIEZOELECTRIC ENERGY HARVESTING MEMS			5. FUNDING NUMBERS
6. AUTHOR(S) Ryan D. Johnson			
7. PERFORMING ORGANIZATION NAME(S) AND ADDRESS(ES) Naval Postgraduate School Monterey, CA 93943-5000			8. PERFORMING ORGANIZATION REPORT NUMBER
9. SPONSORING /MONITORING AGENCY NAME(S) AND ADDRESS(ES) N/A			10. SPONSORING / MONITORING AGENCY REPORT NUMBER

11. SUPPLEMENTARY NOTES The views expressed in this thesis are those of the author and do not reflect the official policy or position of the Department of Defense or the U.S. Government. IRB Protocol number ____N/A____.

12a. DISTRIBUTION / AVAILABILITY STATEMENT Approved for public release; distribution is unlimited	12b. DISTRIBUTION CODE

13. ABSTRACT (maximum 200 words)

Energy conservation and increased efficiency lie at the forefront of defense missions, capabilities, and costs. Expeditionary forces require energy efficient devices embarkable on naval, ground, and air assault vessels. Piezoelectric MEMS (microelectromechanical systems) devices can be used to convert energy—usually lost to mechanical vibrations—into usable electrical energy without adding significant weight or size to existing equipment. Previous work has analyzed materials and processes, and designed a piezoelectric energy harvesting device leading to its fabrication and characterization. This thesis experimentally tests the piezoelectric MEMS device and integrates the results into a refined model. The effects of Rayleigh damping and squeeze film damping are introduced to improve the connection between experimental data and a finite element model using COMSOL Multiphysics. This model exhibits good agreement with experimental results for resonant frequencies and output potential. From this model, the design can be optimized to resonate at 60 Hz.

14. SUBJECT TERMS MEMS, piezoelectric energy harvester			15. NUMBER OF PAGES 63
			16. PRICE CODE
17. SECURITY CLASSIFICATION OF REPORT Unclassified	18. SECURITY CLASSIFICATION OF THIS PAGE Unclassified	19. SECURITY CLASSIFICATION OF ABSTRACT Unclassified	20. LIMITATION OF ABSTRACT UU

NSN 7540–01-280-5500

Standard Form 298 (Rev. 2–89)
Prescribed by ANSI Std. 239–18

THIS PAGE INTENTIONALLY LEFT BLANK

CHARACTERIZATION OF PIEZOELECTRIC ENERGY HARVESTING MEMS

Ryan D. Johnson
Lieutenant Commander, United States Navy
B.S., University of Wisconsin, 2005

Submitted in partial fulfillment of the
requirements for the degree of

MASTER OF SCIENCE IN APPLIED PHYSICS

from the

NAVAL POSTGRADUATE SCHOOL
December 2015

Approved by: Dragoslav Grbovic
                    Thesis Advisor

                    Fabio Alves
                    Co-Advisor

                    Kevin B. Smith
                    Chair, Department of Physics

THIS PAGE INTENTIONALLY LEFT BLANK

ABSTRACT

Energy conservation and increased efficiency lie at the forefront of defense missions, capabilities, and costs. Expeditionary forces require energy efficient devices embarkable on naval, ground, and air assault vessels. Piezoelectric MEMS (microelectromechanical systems) devices can be used to convert energy—usually lost to mechanical vibrations—into usable electrical energy without adding significant weight or size to existing equipment. Previous work has analyzed materials and processes, and designed a piezoelectric energy harvesting device leading to its fabrication and characterization. This thesis experimentally tests the piezoelectric MEMS device and integrates the results into a refined model. The effects of Rayleigh damping and squeeze film damping are introduced to improve the connection between experimental data and a finite element model using COMSOL Multiphysics. This model exhibits good agreement with experimental results for resonant frequencies and output potential. From this model, the design can be optimized to resonate at 60 Hz.

THIS PAGE INTENTIONALLY LEFT BLANK

TABLE OF CONTENTS

THIS PAGE INTENTIONALLY LEFT BLANK

LIST OF FIGURES

LIST OF TABLES

THIS PAGE INTENTIONALLY LEFT BLANK

LIST OF ACRONYMS AND ABBREVIATIONS

AC	alternating current
AlN	aluminum nitride
APS	acoustic power systems
DC	direct current
MEMS	microelectromechanical systems
NPS	Naval Postgraduate School
PZT	lead zirconate titanate
RMS	root mean square
RPM	revolutions per minute
USMC	United States Marine Corps

THIS PAGE INTENTIONALLY LEFT BLANK

ACKNOWLEDGMENTS

THIS PAGE INTENTIONALLY LEFT BLANK

I. INTRODUCTION

The President's Climate Action Plan of 2013 [1] acknowledges the impact of climate change and lays the groundwork for increased energy efficiency, prescribing a shift to clean energy use and reductions in greenhouse gas emissions. Accordingly, the Deputy Secretary of Defense issued the Deputy's Management Action Group Guidance for a Comprehensive Defense Energy Policy [2]. This guidance outlines the critical role energy plays with respect to Department of Defense (DOD) missions, capabilities, and costs [2]. Energy is not simply a commodity; it is a resource to be used for strategic advantage [2]. Energy controls operating environments; it is essential for weapons systems, facilities, and equipment, and represents a significant and fluctuating cost [2]. Therefore, the development of energy-efficient weapons, platforms, and equipment is essential to ensure defense energy security [2]. The United States Marine Corps (USMC) Science and Technology Strategic Plan [3] identifies objectives crucial to future operating forces. Among them, Expeditionary Energy Harvesting is cited as follows, "Develop cost effective and efficient capabilities to harvest energy from the sun, battlefield waste, vehicles, and personnel. Technologies must be embarkable aboard naval shipping and transportable aboard ground and air assault transportation." [3, p. 30]. According to the National Electrical Manufacturer's Association (NEMA) [4], the United States lost more energy due to inefficiency than it consumed in 2011. Clearly, energy efficiency will play a pivotal role in our nation's future economic success and national security.

The piezoelectric energy harvesting industry is forecasted to be worth over $800 million in the next 10 years [5]. Over 200 piezoelectric materials are available for specific applications, including consumer electronics, healthcare, aerospace, military, and pavement, roads, and railways [5]. Piezoelectric energy harvesters can be used to convert ambient vibrations into electrical energy for storage or as a supply to numerous electrical devices [6]. It has been demonstrated that piezoelectric energy harvesters have recharged nickel metal hydride batteries and are also becoming an attractive alternative for powering microelectromechanical systems (MEMS) devices, sensors, and actuators [6]. Piezoelectric MEMS energy harvesters therefore have the ability to recapture wasted energy from

vehicles and personnel, and improve system efficiency with little impact on the mobility of expeditionary forces as required by the USMC.

A.   BACKGROUND

This thesis is a continuation of the work performed by LT Daniel Hogue and LT Sarah Gregory [7], LCDR Timothy Householder [8], and LT Seyfullah Emen [9]. Initially, a piezoelectric MEMS device employing a cantilever configuration was designed using COMSOL Multiphysics software. The goal was to obtain a structure that would resonate at 60 Hz to take advantage of the normal operation of a shipboard gas turbine engine rotating at 3600 RPM and other 60 Hz AC electronics [7]. Meanwhile, the microfabrication process was studied using the Naval Postgraduate School (NPS) cleanroom facilities to determine optimal techniques for fabricating devices able to harvest waste energy from vibrational sources [7]. Subsequent design modification, material characterization, and experimental testing using acoustic and vibrational actuation brought forward proof of concept [8]. To further improve finite element model accuracy, Householder [8] determined the actual values of Young's modulus and layer thicknesses. In addition, circuit analysis of array configuration and power conditioning was performed to determine optimal power output [9].

B.   SCOPE

The objective of the research, reported in this thesis, is to experimentally analyze the performance of previously fabricated MEMS piezoelectric energy harvesters and use the results to optimize an advanced finite element model to be used in future device designs. A piezoelectric device designed by Gregory [7] and Householder [8], and fabricated by a commercial foundry, MEMSCap, is actuated by a vibrational shaker and analyzed to determine resonance and output potential. The experimental setup is modified from previous work to accurately capture the physical displacement of the device and film the modes of resonant excitation using high-speed photography. Using the physical device parameters and experimental data, finite element models from previous work are modified using COMSOL Multiphysics 5.1. The mass, stiffness, and squeeze-film damping parameters are also investigated to match the model to truth.

II.   PRINCIPLES OF OPERATION

A.   PIEZOELECTRIC EFFECT

The piezoelectric effect, discovered by Pierre and Jacques Curie in 1880, is the generation of an electric charge in specific materials when mechanically stressed [10]. This is referred to as the direct effect of piezoelectricity, and conversely these materials will mechanically deform when subjected to an electric field, the inverse effect of piezoelectricity [10]. For example, quartz is a naturally occurring piezoelectric material that when subjected to an electric field of 1000 V/cm experiences a strain of 10^{-7}; meaning a very small strain may cause a significant electric field [10]. For the direct effect of piezoelectricity, the electrical polarization is related to the applied mechanical stress by

$$D = dT + \varepsilon E, \tag{1}$$

where D is the electrical polarization, d is the piezoelectric coefficient matrix, T is the applied mechanical stress, ε is the electrical permittivity matrix, and E is the electric field [10]. For the indirect effect of piezoelectricity, the strain is related to the applied electric field and mechanical stress by

$$s = ST + dE, \tag{2}$$

where s is the total strain and S is the compliance matrix [10]. In order for a material to exhibit the effects of piezoelectricity it must be a noncentrosymmetric crystal, meaning it lacks symmetry along all axes through its center [10]. This allows ionic charges to become displaced under stress creating a polarization and consequently an electric field [10]. Materials of particular interest to this work include PZT (lead zirconate titanate) and AlN (aluminum nitride). Although PZT is widely used for its high piezoelectric strain coefficient and dielectric constant, it is also brittle and therefore less attractive for use as a vibrational energy harvester [7]. AlN was chosen for its compatibility with semiconductor technology fabrication processes and good piezoelectric properties that remain constant over a wide range of temperatures [7].

B. MICROELECTROMECHANICAL SYSTEMS

Microelectromechanical systems (MEMS) were born out of integrated circuit technology and the strong push for innovation [10]. The advantages of MEMS are found in its miniaturization, microelectronics integration, and parallel fabrication. Miniaturization refers to a length scale ranging from just 1 micron to 1 cm, leading to scaling law benefits such as softer springs and greater sensitivity, particularly useful for energy harvesting [10]. Seamless integration of mechanical sensors with electrical controllers allows MEMS devices to be combined into a single product. In addition, the ability to realize tiny dimensions with precision using new micromachining processes that traditional methods cannot achieve makes MEMS devices truly remarkable and versatile [10].

C. PIEZOELECTRIC ENERGY HARVESTING MEMS

Combining the piezoelectric effect with the advantages of MEMS allows for the creation of piezoelectric energy harvesting devices that provide a negligible impact on the space and weight considerations of deployable assets. A basic cantilever piezoelectric energy harvesting MEMS device is shown in Figure 1 [11].

Figure 1.   Basic Piezoelectric Energy Harvesting MEMS Device
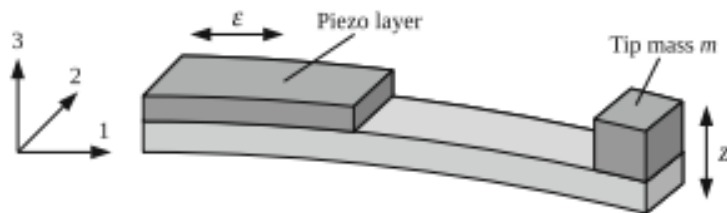
The basic cantilever piezoelectric energy harvester is fixed at one end and free to bend at the other. It consists of a layer of piezoelectric material deposited along a layer of elastic material [11]. A tip mass is typically added at the end of the cantilever for increased strain and output potential as well as resonance frequency control [11]. Source: T. Hehn and Y. Manoli, *CMOS Circuits for Piezoelectric Energy Harvesters*. Dordrecht, Netherlands: Springer Netherlands, 2015, pp. 21–39.

The cantilever in Figure 1 could be fixed to a vibrational source at one end and allowed to oscillate freely at the other. Because piezoelectric material is fairly stiff, a thin

layer is usually deposited along an elastic material to reduce the resonance frequency to the range of ambient vibrations [11]. A tip mass is added at the end of the cantilever for increased strain and output potential, as well as to reduce the resonant frequency [11]. In this configuration, the cantilever oscillates significantly in the 3-direction creating a small strain within the piezoelectric material along the 1-direction [11]. Because of the 31-mode crystal orientation, a potential difference will exist orthogonal to the applied stress [11]. The output potential of the device is determined by grounding the elastic material and attaching an electrical contact terminal to the top of the piezoelectric material.

An equivalent mechanical model of a piezoelectric energy harvester is shown in Figure 2 [11]. The vibrating frame position is represented by $y(t)$ and the piezoelectric energy harvester position is represented by $z(t)$ [11]. The mass of the harvester is m, k_s is the spring constant, d is the damping, F_e is the restoring force, and V and I are the voltage and current produced by the harvester connected to an interface circuit [11].

Figure 2.   Equivalent Mechanical Model of a Piezoelectric Energy Harvester
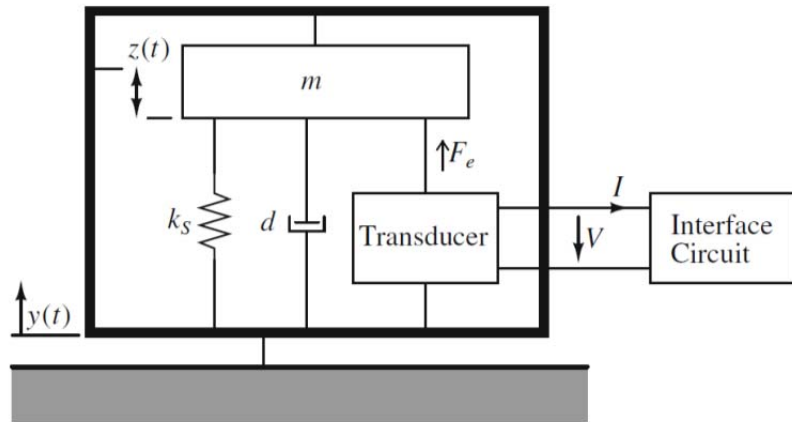
Spring-mass-damper equivalent representation of a piezoelectric energy harvester. The vibrating frame position is represented by $y(t)$ and the piezoelectric energy harvester mass position is represented by $z(t)$. The mass is m, k_s is the spring constant, d is the damping, F_e is the restoring force, and V and I are the voltage and current of the harvester. Source: T. Hehn and Y. Manoli, *CMOS Circuits for Piezoelectric Energy Harvesters*. Dordrecht, Netherlands: Springer Netherlands, 2015, pp. 21–39.

An equivalent electrical circuit of a piezoelectric energy harvester is shown in Figure 3 [8]. The capacitor, C, represents the stiffness, the inductance, L, represents the mass, and the resistor, R, represents the damping of the harvester [8]. C_o represents the capacitance of the electrodes in parallel with the harvester and Z_L represents the load connected to the harvester [8].

Figure 3.   Equivalent Electrical Circuit of Piezoelectric Energy Harvester
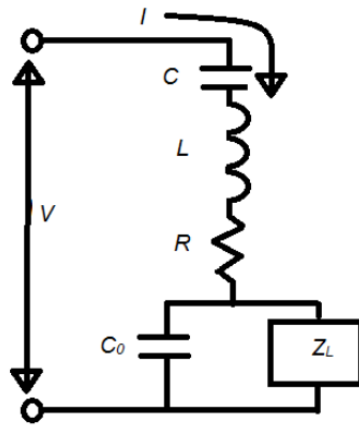
Equivalent LRC electrical circuit of the piezoelectric energy harvester. The capacitance serves as the spring stiffness, the inductance represents mass, and the resistance represents damping. Source: T. J. Householder, "MEMS-based waste vibration and acoustic energy harvesters," M.S. thesis, Dept. Physics, Naval Postgraduate School, Monterey, CA, 2014.

III. PREVIOUS WORK

A. HOGUE AND GREGORY

Hogue and Gregory [7] began the project by designing a piezoelectric energy harvesting device using COMSOL Multiphysics modeling software. The initial design, utilizing the concepts of Chapter II, was inspired by an earlier NPS thesis exploring the possibilities of using solar power and the piezoelectric effect to harvest energy [12]. The design goal was to develop an energy harvester with a resonant frequency of 60 Hz [7]. The resonant frequency of a simple harmonic oscillator is given by

$$\omega = 2\pi f = \sqrt{\frac{k}{m}},$$

(3)

where ω is the angular frequency, f is the frequency, k is the spring constant, and m is the mass. Therefore, to reduce the resonant frequency to 60 Hz, the spring constant must be reduced. Here the scaling law of the spring constant (spring constant is proportional to length) and the inherent MEMS advantage of miniaturization play a key role as cantilevers of reduced size produce softer springs [10]. The spring constant can further be defined as

$$k = \frac{Ewt^3}{4l^3},$$

(4)

where E is the modulus of elasticity, w is the width of the beam, t is the thickness, and l is the length for a fixed-free cantilever loaded normal to the substrate [10]. The initial design utilized six multi-fold legs to increase the effective length of the cantilever system to reduce the spring constant and achieve the frequency goal as shown in Figure 4. This design involved a thin layer of AlN over silicon, with an additional aluminum layer over the center pad area (320 μm X 460 μm rectangle) [7]. Figure 5 is a scanning electron microscope image of the first generation design.

Figure 4.   First Generation Piezoelectric Energy Harvester
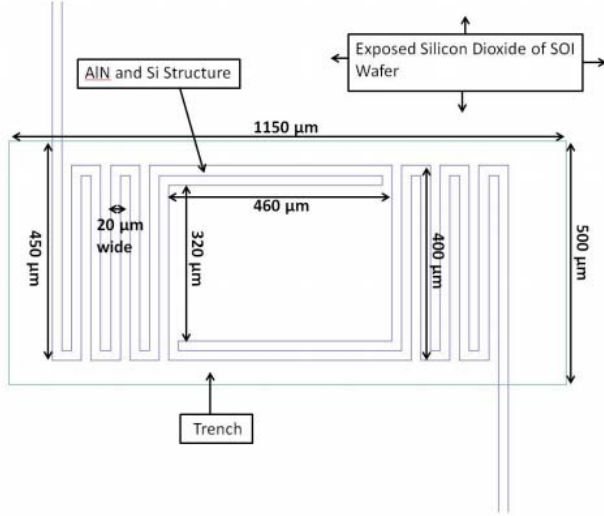
First generation piezoelectric energy harvester with six multi-fold legs to increase the effective length of the cantilevers for reduced resonance frequency. Source: D. B. Hogue and S. M. Gregory, "MEMS-based waste vibrational energy harvesters," M.S. thesis, Dept. Physics, Naval Postgraduate School, Monterey, CA, 2013.

Figure 5.   Scanning Electron Microscope Image of First Generation
Piezoelectric Energy Harvester
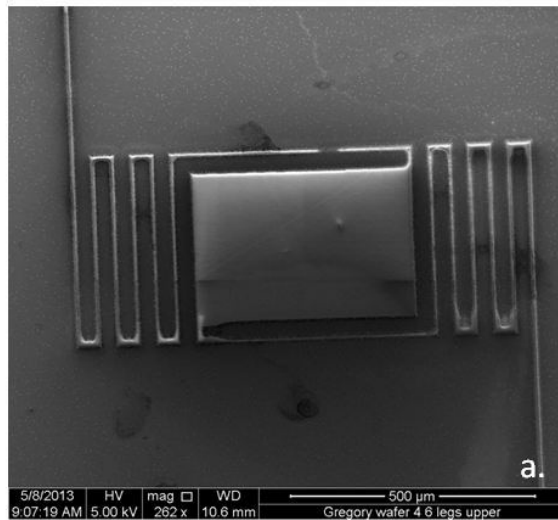
Scanning electron microscope image of first generation piezoelectric energy harvester designed by Gregory [7] to resonate at 60 Hz. The harvester consisted of six multi-fold legs connected to a center pad. Source: D. B. Hogue and S. M. Gregory, "MEMS-based waste vibrational energy harvesters," M.S. thesis, Dept. Physics, Naval Postgraduate School, Monterey, CA, 2013.

AlN was the piezoelectric material chosen for this design based on advantageous metal deposition techniques and compatibility with standard semiconductor fabrication technology [7]. The piezoelectric properties of AlN are also relatively constant over a wide range of temperatures [7]. AlN was further characterized using scanning electron microscopy, etch-rate analysis, and x-ray diffraction to confirm crystal orientation. The pebble-type topography visible from the scanning electron microscope and the measured diffraction pattern indicated a high c-axis orientation [7]. C-axis orientation is optimal in this application because the electric field produced will be orthogonal to the applied stress [7].

B.   HOUSEHOLDER

Unfortunately the original design was unable to survive shipment after fabrication by MEMSCap, requiring Gregory [7] and Householder [8] to continue the project with design modifications. The oscillation of the devices exceeded the width of the substrate, causing the device to adhere to shipping tape [8]. Subsequent attempts to free the devices resulted in fracture [8]. Therefore, a more robust piezoelectric energy harvester design was required, resulting in an increased resonant frequency [8]. Figure 6 shows the design evolution and the final two-leg piezoelectric energy harvester used for experimental testing (third generation). The entire footprint of the designed device is about 4 mm by 4.5 mm.

Figure 6.   Design Evolution of the Piezoelectric Energy Harvester
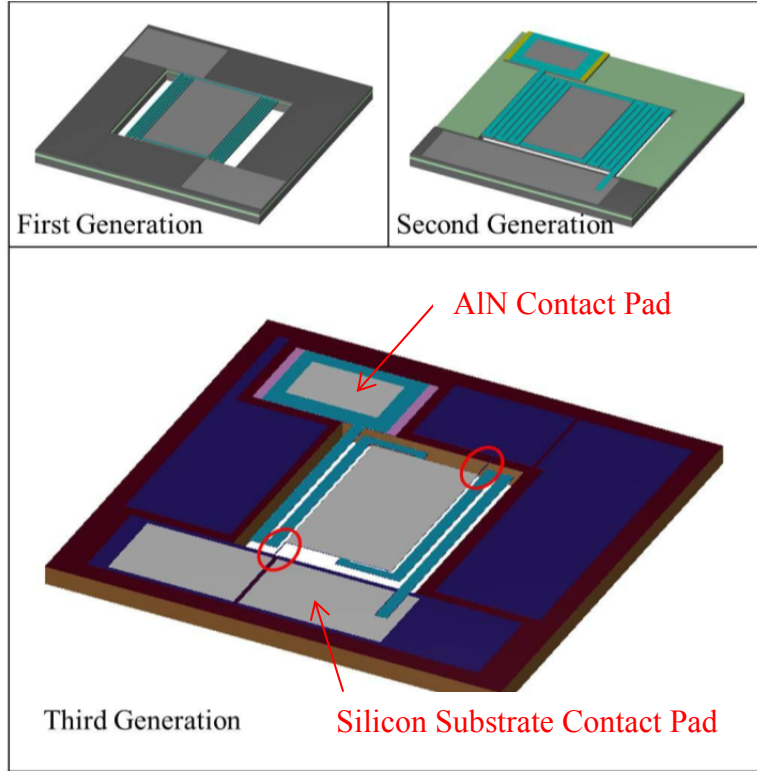
The first generation device consisted of six multi-fold legs on each side of a center pad. The legs and center pad consisted of a layer of silicon covered with a thin layer of piezoelectric AlN. The center pad featured an additional layer of aluminum as an added proof mass to reduce the resonant frequency. The second generation maintained six multi-fold legs, but increased the width of the legs for structural support. The third generation design shifted to two multi-fold legs of increased width. Additionally, small temporary bridge structures (circled in red) were added to aid in shipment survival. These bridges are later broken to free the device in preparation for testing. Source: T. J. Householder, "MEMS-based waste vibration and acoustic energy harvesters," M.S. thesis, Dept. Physics, Naval Postgraduate School, Monterey, CA, 2014.

The two-leg piezoelectric energy harvester was tested using both acoustic and vibrational testing. While acoustic testing showed no clear resonance and low output voltages, the vibrational testing did lead to a resonance at 380 Hz producing 2.4 mV$_{rms}$ as measured by an oscilloscope [8]. The spike in output potential and characteristic 180 degree phase shift at 380 Hz is visible in Figure 7.

Figure 7.   Householder Vibrational Testing Results
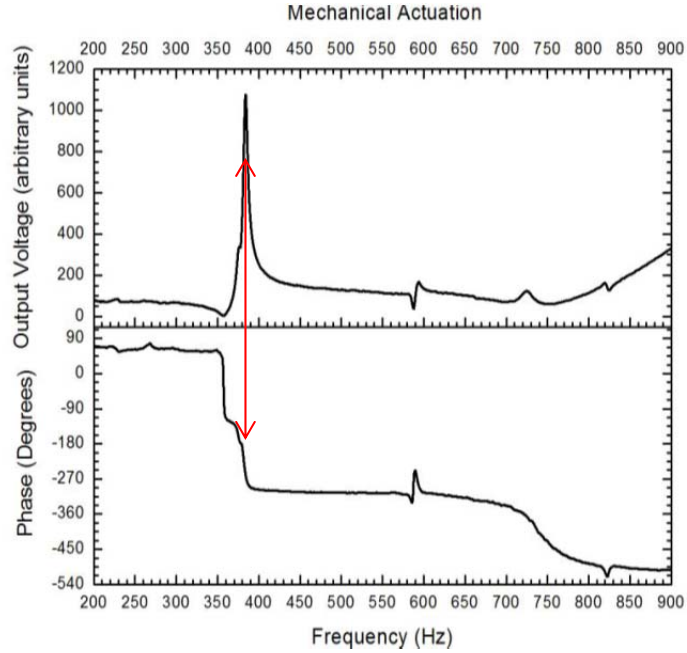
The resonance point is indicated by the red arrow showing the connection between the output voltage spike and a 180 degree phase shift occurring at 380 Hz. Source: T. J. Householder, "MEMS-based waste vibration and acoustic energy harvesters," M.S. thesis, Dept. Physics, Naval Postgraduate School, Monterey, CA, 2014.

Additional material characterization was performed to determine the layer thickness and Young's modulus. Using a KLA Tencor D120 Contact Profilometer, Filmetrics F40 Spectroscopic Thickness Measurement Instrument, and Zygo Nanoview 7100 Optical Profilometer, the silicon substrate, AlN piezoelectric layer, and aluminum center pad thicknesses were precisely measured at 10, 0.493, and 1 micron, respectively (10, 0.500, and 1.02 micron design) [8]. The Young's modulus of silicon was experimentally determined to be 173.3 GPa (180 GPa theory), and AlN was experimentally measured at 384.0 GPa (331 GPa theory) using an Agilent Nano Indenter G200 [8]. Rayleigh damping was explored as a mechanism for modeling mass and stiffness damping of the piezoelectric energy harvester, and the finite element model in COMSOL Multiphysics was adjusted to further its accuracy.

C.   EMEN

Emen performed vibrational testing on a second device equivalent to Householder's and discovered resonance at 665 Hz, producing 19 mV$_{rms}$ [9]. The difference between these observations is shown in Figure 8 and discussed in Chapter IV.

Figure 8.   Householder and Emen Piezoelectric Energy Harvester Resonance Comparison
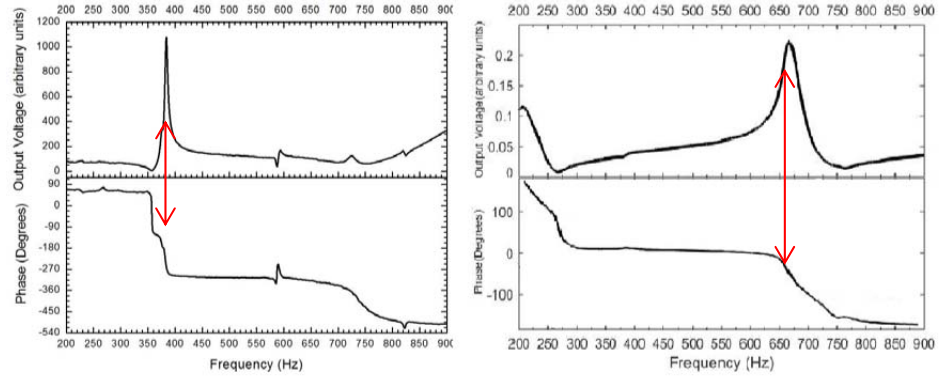
The resonance point is indicated by the red arrows showing the connection between the output voltage spikes and a 180 degree phase shift occurring at 380 Hz in [8], but 665 Hz in [9]. Source: S. Emen, "Power conditioning for MEMS-based waste vibrational energy harvester," M.S. thesis, Dept. Physics, Naval Postgraduate School, Monterey, CA, 2015.

Parallel vs. series array configurations with power conditioning circuits was explored using LTSPICE IV simulation software and the internal impedance of the piezoelectric energy harvester was determined to be equivalent to an 828 pF capacitor [9].

IV. EXPERIMENTAL RESULTS

The experimental results reported by Householder [8] and Emen [9] were inconsistent and required further evaluation. It was discovered that the device tested by Householder [8] was secured at the opposite end of the aluminum base plate from the harvester. This caused the harvester to experience additional vibrations as the aluminum mounting plate vibrated on the mechanical shaker. The interference between the vibrations of the shaker and the vibrations of the aluminum mounting plate may have been the cause for the discrepancy between the resonant data reported by Householder [8] and Emen [9]. Unfortunately both devices were fractured in non-testing related events. Therefore, an additional third generation piezoelectric energy harvester was prepared for testing to resolve the discrepancy in resonance frequency and output potential. Additionally, no characterization of the mechanical shaker used for testing was performed, meaning there was no information available about the magnitude of displacement experienced by the harvester under test. Consequently, the experimental setup was adjusted to obtain this information.

A. EXPERIMENTAL SETUP

The experimental setup used in this work and shown in Figure 9 is very similar to the ones described and used by Householder [8] and Emen [9]. However, modifications were incorporated to characterize the mechanical shaker and capture high-speed images to observe the modes of excitation at different resonant frequencies. The main modification was the addition of a signal conditioner, necessary to convert the charge per unit acceleration sensed by the accelerometer into an output voltage. It is important to note the connection of the accelerometer to the signal conditioner for proper operation. The output of the accelerometer was connected to the rear panel input PE (piezoelectric) of the signal conditioner. The rear panel output AC of the signal conditioner was then routed to an input on either the lock-in amplifier or the oscilloscope for monitoring and recording. The main settings for the lock-in amplifier, signal conditioner, and imaging software are tabulated in Appendix A.

13

Figure 9.   Experimental Setup Block Diagram
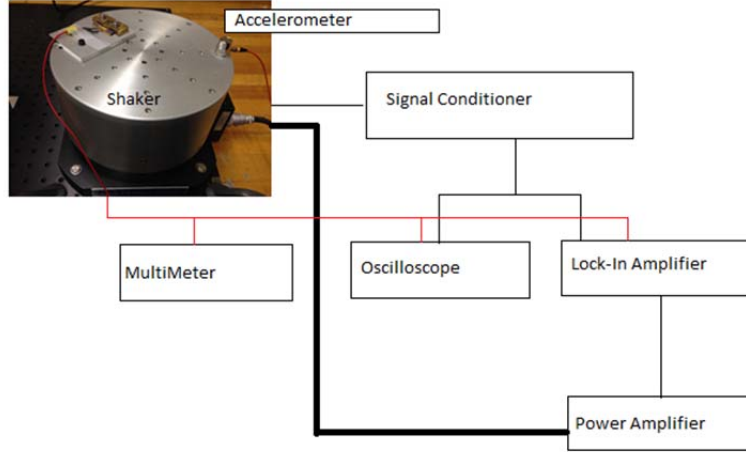
The block diagram illustrates the wiring connections between experimental instruments and the piezoelectric energy harvester. Adapted from T. J. Householder, "MEMS-based waste vibration and acoustic energy harvesters," M.S. thesis, Dept. Physics, Naval Postgraduate School, Monterey, CA, 2014.

The piezoelectric energy harvester designed by Gregory [7] and Householder [8] was mounted on an Acoustic Power Systems (APS) Permadyne Model 120S Shaker using a brass plate bonded to a thin aluminum plate as shown in Figure 10. There is a 1 mm cavity in the brass plate beneath the harvester to allow for oscillation. Gold wire bonding between the piezoelectric energy harvester and a ceramic integrated circuit package was performed using a Kulicke & Soffa 4524A Digital Manual Wire Bonder. This allowed electrical connections between the device and the measurement instruments. Placement of the ceramic integrated circuit package as close to and in the same plane as the harvester is necessary to reduce the wire-bond length and improve bonding success. Securing the brass plate to the shaker near the harvester is also important to ensure the harvester experiences the true vibration of the mechanical shaker.

Figure 10.   Piezoelectric Energy Harvester Mounted on Mechanical Shaker
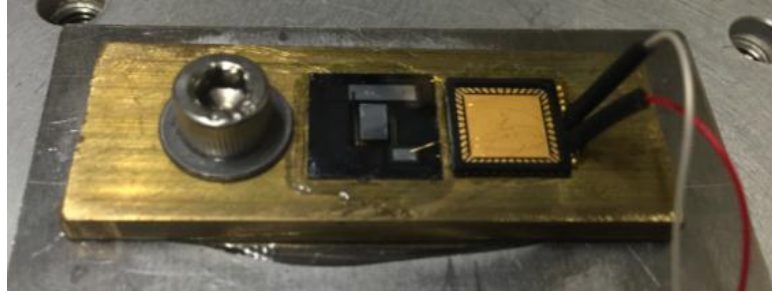
The piezoelectric energy harvester, located in the center, was super-glued onto a brass plate with a 1 mm cavity beneath. The ceramic integrated circuit package on the right was mounted a close as possible to and in the same plane as the harvester to minimize the distance of the wire-bonding. The mounting plate was bolted to the shaker to the left of the harvester to ensure the harvester experiences the true input vibration of the shaker.

An overview of the complete experimental setup is shown in Figure 11 (equipment identified as (a) through (h)). The mechanical shaker (a) provided the vibration governed by an APS Dual-Mode Power Amplifier Model 114 (b) operating in the current mode, designed for applications involving modal test excitation [13]. The amplifier received a driving signal from a Stanford Research Systems Model SR850 DSP Lock-In Amplifier (c), utilized for its ability to detect AC signals as low as a few nanovolts hidden in noise [14]. The lock-in amplifier was used to both supply a driving voltage to the power amplifier and measure the phase and output voltage of the piezoelectric energy harvester and the accelerometer, also mounted on the shaker. An Endevco 7701A-100 Isoshear Accelerometer (d) was used with an Endevco Signal Conditioner Model 2775A (e) for the purpose of converting a charge measured by the accelerometer to a voltage. This conversion is necessary to determine the acceleration and/or displacement experienced by the shaker and the piezoelectric energy harvester. The output of the piezoelectric energy harvester was also measured using a Tektronix DPO2012 Digital Phosphor Oscilloscope (f) and a Fluke 85 III True RMS Multimeter (not pictured). High-speed imaging of the piezoelectric energy harvester was recorded at resonance using a Redlake MotionPro X3 High-Speed Motion Camera with a Carl Zeiss AG Makro-Planar T* 2/100mm ZF.2 Lens (g). Image processing was accomplished using MotionStudio Image Acquisition and Processing software (not pictured). A spotlight (h) was also necessary to improve lighting conditions given the short exposure time (997 μs).

Figure 11.　Experimental Setup Overview
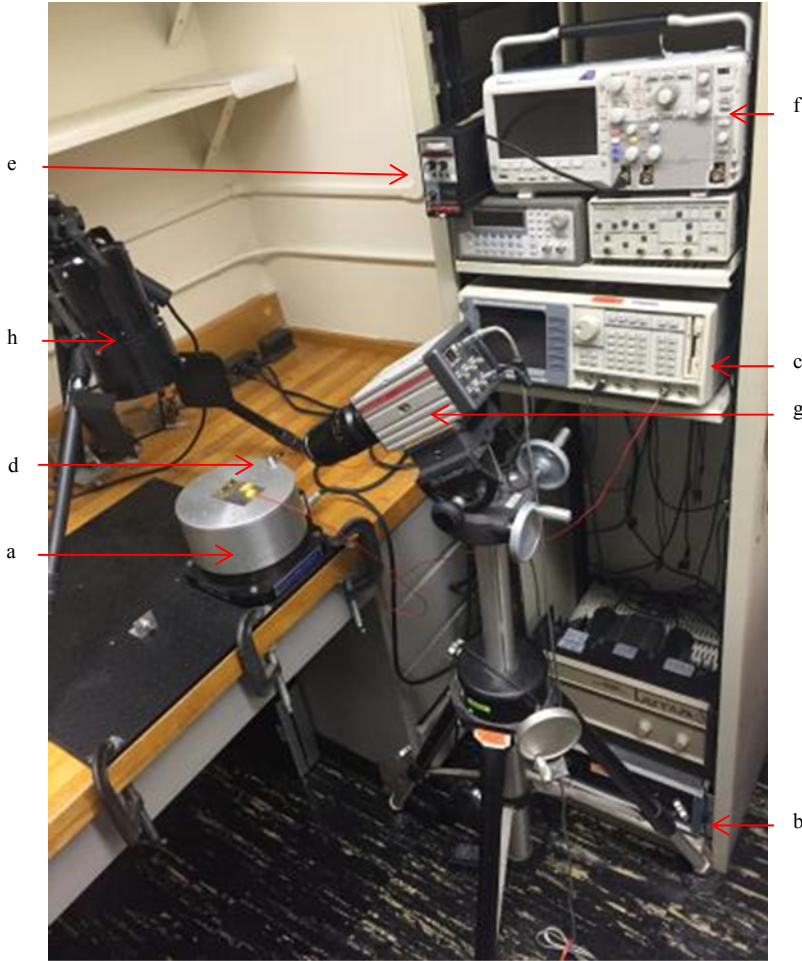
The image above demonstrates the necessary angle and proximity of equipment necessary to capture usable high-speed video. (a) APS Permadyne Model 120S Shaker, (b) APS Dual-Mode Power Amplifier Model 114, (c) Stanford Research Systems Model SR850 DSP Lock-In Amplifier, (d) Endevco 7701A-100 Isoshear Accelerometer, (e) Endevco Signal Conditioner Model 2775A, (f) Tektronix DPO2012 Digital Phosphor Oscilloscope, (g) Redlake MotionPro X3 High-Speed Motion Camera with a Carl Zeiss AG Makro-Planar T* 2/100mm ZF.2 Lens, (h) spotlight.

B.　INTRINSIC STRESS

A Zygo NanoView 7100 Optical Profilometer was used to produce a three dimensional image of the piezoelectric energy harvester under test. The image shows the intrinsic stress within the material resulting in the curved appearance visible in Figure 12 and typical of many MEMS devices. This is normal and similar to the devices tested by Householder [8] and Emen [9]. Note that the deformation has been exaggerated to clearly

depict relative deformation of various parts of the harvester. The surface color represents displacement in the z-direction (vertical). Red indicates the greatest amount of deformation; blue indicates the least amount of deformation. This indicates that the center pad is curved concave up in the z-direction at rest, which may affect the stiffness of the harvester [10].

Figure 12.   Zygo NanoView 7100 Optical Profilometer 3-Dimenisonal Image
of Piezoelectric Energy Harvester Under Test
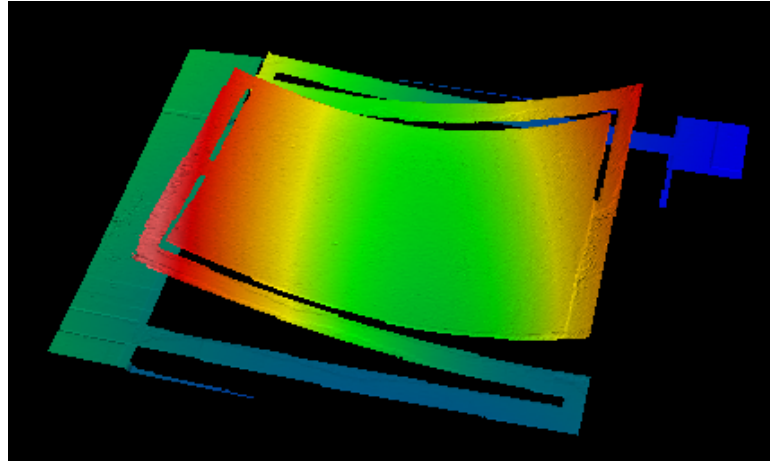
The surface color represents displacement in the z-direction that has been exaggerated to clearly identify regions of increased relative deformation. Red indicates the greatest amount of deformation; blue indicates the least amount of deformation. This indicates that the center pad is curved concave up in the z-direction, causing the multi-fold legs to bend upward at rest.

C.   INTERNAL IMPEDANCE

A multimeter was used to compare the internal impedance of the piezoelectric energy harvesters. The impedance of the device tested by Emen [9] was measured at 290 kΩ, whereas the impedance of the device used for this work was measured at 297 kΩ. The small variation is most likely due to increased oxidation of the harvester used in this work because of the added time it was exposed to ambient conditions. An impedance measurement for the harvester tested by Householder [8] was unavailable due to a non-testing related fracture.

D. MECHANICAL SHAKER CHARACTERIZATION

The mechanical shaker was driven by the lock-in amplifier with a 0.1 V_{rms} sinusoidal waveform and the output potential of the accelerometer was measured using the signal conditioner. A frequency sweep from 100 to 1000 Hz was performed and the plot of output potential is presented in Figure 13. Frequency sweeps below 100 Hz were avoided because of the excessive noise and building vibration they produced. Frequency sweeps were limited to 1000 Hz because of the limits of the power amplifier [13]. The output of the accelerometer is roughly steady beyond 200 Hz, but exhibits a sharp anti-resonant negative spike near 120 Hz. The average value of the potential between 200 and 1000 Hz was calculated at 0.182 V_{rms}, and is used as an input parameter to the finite element model in Chapter V.

Figure 13.   Endevco Accelerometer Output Potential vs. Frequency
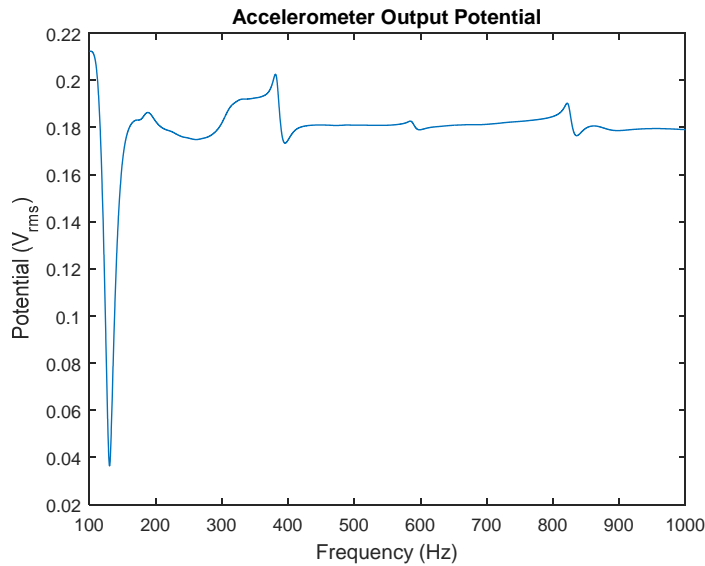
The ouput of the accelerometer is roughly steady beyond 200 Hz, but exhibits a sharp anti-resonant negative spike near 120 Hz. The average value of the potential between 200 and 1000 Hz was calculated at 0.182 V_{rms}. This average value is used to determine the input parameter, prescribed acceleration, used in the finite element model in Chapter V.

The signal conditioner was set to a full scale output peak voltage of 1.0 V_{pk}. The full scale acceleration range was set to 10 g, where g is the peak gravitational acceleration (1 g = 9.81 m/s^2). Therefore, the system sensitivity as given by [15] is

18

$$SystemSensitivity = \frac{FullScaleOutput[V_{pk}]}{FullScaleRange[g_{pk}]} = 0.1 \left[\frac{V_{pk}}{g_{pk}}\right] \qquad (5)$$

According to [15] the acceleration experienced by the shaker is given by

$$Acceleration\left[g_{pk}\right] = \frac{PeakACVoltageOut[V_{pk}]}{SystemSensitivity\left[\dfrac{V_{pk}}{g_{pk}}\right]} \qquad (6)$$

The displacement, *z(t)*, can be calculated by integrating the acceleration twice as follows in equation set (7).

$$a(t) = A\sin(\omega t)$$

$$v(t) = \int a(t)dt = -\frac{A}{\omega}\cos(\omega t) \qquad (7)$$

$$z(t) = \int v(t)dt = -\frac{A}{\omega^2}\sin(\omega t)$$

Therefore, the magnitude of the displacement equals the acceleration divided by the angular frequency squared. MATLAB 2015a was used to perform this conversion from acceleration to displacement and the results are available in Figure 14. The Endevco Signal Conditioner Model 2775A equations and subsequent integration produced the relationship that displacement is proportional to acceleration divided by the square of frequency, as expected. Once again, the anti-resonance at 120 Hz produces a sharp negative spike. Note the displacement is 1.4 µm at 669 Hz, and 20.6 µm at 177 Hz, corresponding to the resonant frequencies observed later within this chapter (Section E). This procedure and plot characterizes the actual displacement experienced by the piezoelectric energy harvester for the experimental lock-in amplifier driving voltage, and will be used as an input parameter in the finite element model, described in Chapter V.

Figure 14.   Endevco Accelerometer Displacement vs. Frequency
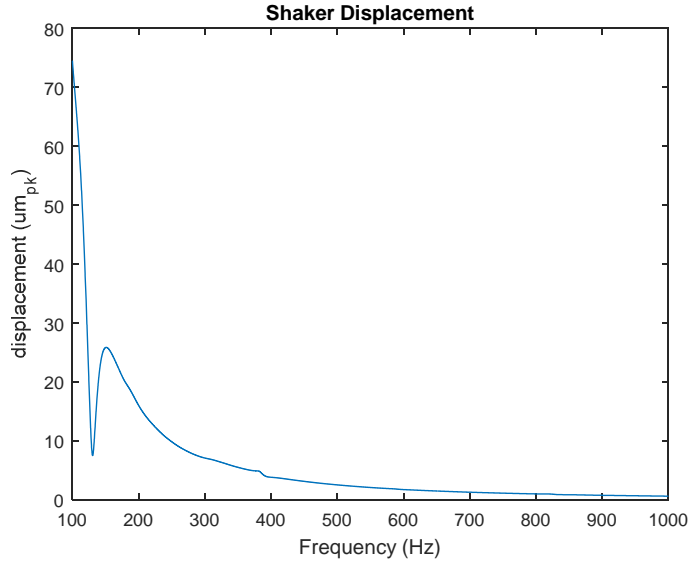
The Endevco Signal Conditioner Model 2775A equations and subsequent integration produced the relationship that displacement is proportional to acceleration divided by the square of frequency as expected. Once again, the anti-resonance at 120 Hz produces a sharp negative spike. For future note, the displacement is 1.4 μm at 669 Hz, and 20.6 μm at 177 Hz.

E.   VIBRATIONAL TESTING

The lock-in amplifier was used to measure the potential and phase of the piezoelectric energy harvester as a function of frequency. Figures 15, 16 and 17 indicate resonance at 177 Hz and 669 Hz. Note that the peak in potential at 177 Hz and 669 Hz corresponds roughly to a 180 degree phase shift as expected at resonance. The peak potential measured by the lock-in amplifier was 15.1 mV$_{rms}$ at 669 Hz. The frequency sweep from 100–1000 Hz was chosen because the shaker is limited to 1000 Hz and frequencies below 100 Hz caused significant noise and vibration of the building.

Figure 15.   Piezoelectric Energy Harvester Output Potential vs. Frequency
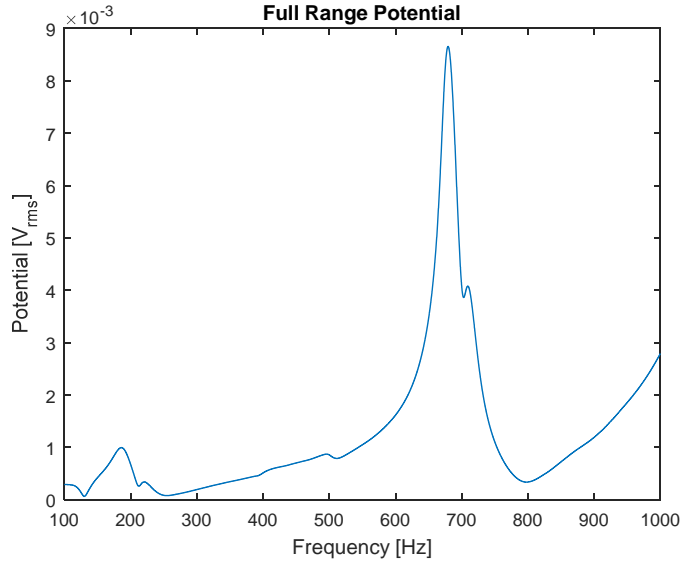
The output potential of the piezoelectric energy harvester exhibited two resonant peaks, one at 177 Hz and the other at 669 Hz. The frequency sweep from 100–1000 Hz was chosen because the shaker is limited to 1000 Hz and frequencies below 100 Hz caused significant noise and vibration of the building.

A frequency sweep from 615 to 725 Hz was performed to accurately determine the maximum RMS output potential of the harvester around 669 Hz. This provided a +/- 50 Hz window around resonance to view the expected connection, as indicated by the red arrows, between the resonant voltage spike and an approximate 180 degree phase shift. An output potential of 15.1 mV$_{rms}$ was measured at 669 Hz. This result closely matches the 665 Hz resonance and 19 mV$_{rms}$ reported by Emen [9].

Figure 16.   Piezoelectric Energy Harvester Output Potential vs. Frequency
Focusing on Resonance at 669 Hz
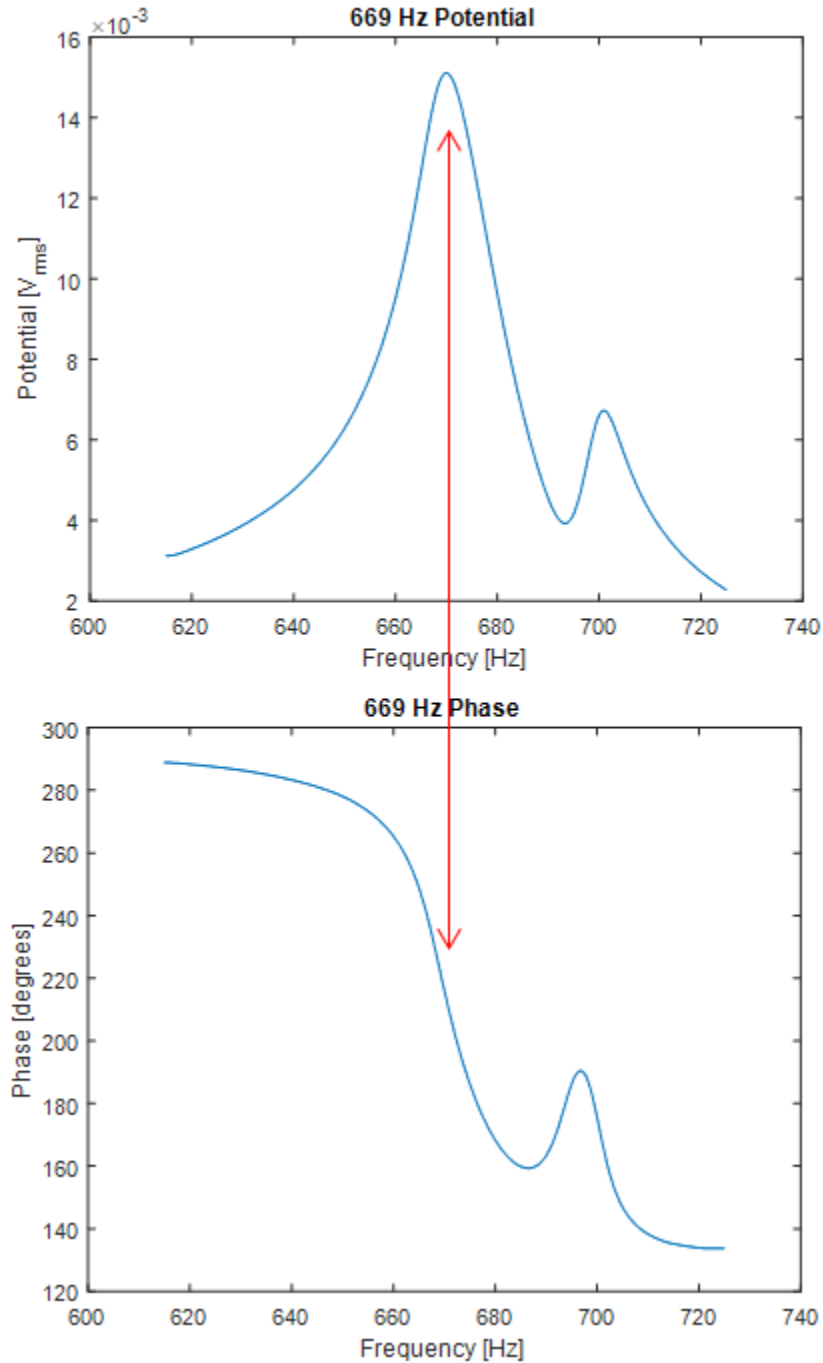
A frequency sweep from 615 to 725 Hz was performed to accurately determine the maximum RMS output potential of the harvester around 669 Hz. This provided a +/-50 Hz window around resonance to view the expected connection, as indicated by the red arrows, between the resonant voltage spike and an approximate 180 degree phase shift. An output potential of 15.1 mV$_{rms}$ was measured at 669 Hz.

A frequency sweep from 150 to 250 Hz was performed to accurately determine the maximum RMS output potential of the harvester around 177 Hz. This provided a 100 Hz window around resonance to view the expected connection, as indicated by the red arrows, between the resonant voltage spike and an approximate 180 degree phase shift. An output potential of 4.5 mV$_{rms}$ was measured at 177 Hz.

Figure 17.   Piezoelectric Energy Harvester Output Potential vs. Frequency Focusing on Resonance at 177 Hz
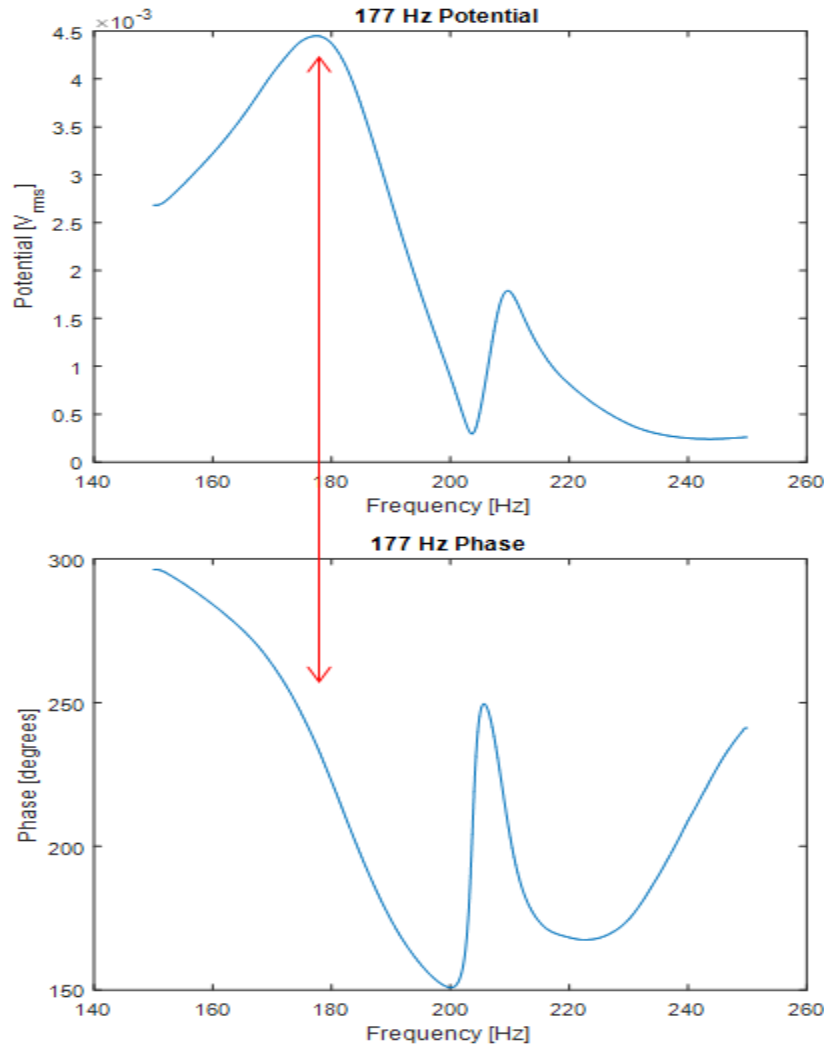
A frequency sweep from 150 to 250 Hz was performed to accurately determine the maximum RMS output potential of the harvester around 177 Hz. This provided a 100 Hz window around resonance to view the expected connection, as indicated by the red arrows, between the resonant voltage spike and an approximate 180 degree phase shift. An output potential of 4.5 mV$_{rms}$ was measured at 177 Hz.

The piezoelectric energy harvester was also connected to an oscilloscope and a multimeter, and a manual frequency sweep from 625–715 Hz was performed for comparison with the lock-in amplifier. The oscilloscope indicated resonance at 664 Hz with a peak voltage of 11.8 mV$_{rms}$, while resonance was observed at 664 Hz and 17.4 mV$_{rms}$ using the multimeter. A comparison is presented in Figure 18. All three measuring instruments are in close agreement with respect to the resonant frequency and output potential. Variations in the peak voltage are most likely attributable to the difference in input impedance of the measuring device. The internal impedance of the oscilloscope consists of a 1 MΩ resistor in parallel with an 11.5 pF capacitor, whereas the internal impedance of the multimeter consists of a 10 MΩ resistor in parallel with a 100 pF capacitor. The difference in the output potential indicates the dependence of the harvester output potential on load impedance, as discussed by Hogue and Gregory [7].

Figure 18.   Piezoelectric Energy Harvester Output Potential vs. Frequency as Measured by the Oscilloscope and Multimeter
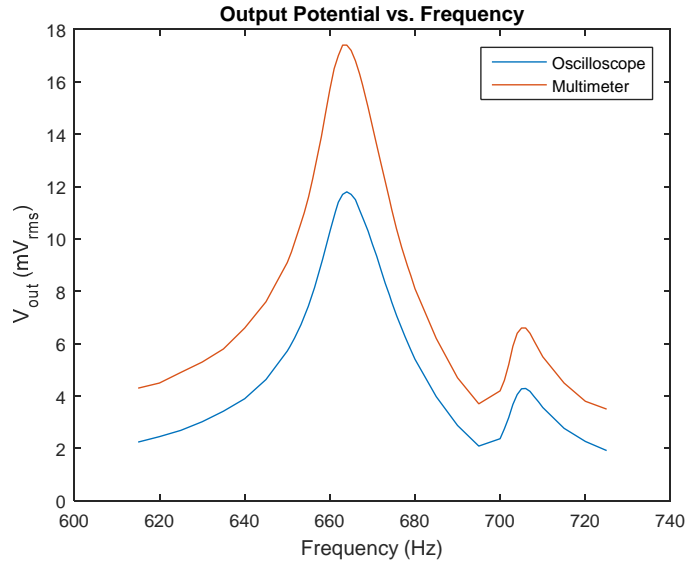
A manual frequency sweep was performed from 615 to 725 Hz and the output voltage of the harvester was recorded using an oscilloscope and multimeter for comparison with the lock-in amplifier data. The oscilloscope data indicated a resonance output voltage of 11.8 mV$_{rms}$ at 665 Hz, while the multimeter indicated a resonance output voltage of 17.4 mV$_{rms}$ at 665Hz. The difference in the output potential is due to the varying input impedance among the three measuring instruments and indicates the dependance of harvester output potential on load impedance [7].

F.   RAYLEIGH AND SQUEEZE-FILM DAMPING

Damping was required to be incorporated into the finite element model to simulate mass, stiffness, and thin film squeeze damping of the resonant motion of the piezoelectric energy harvester. Damping must be analyzed to account for the electromechanical energy lost between the vibrational source and the final electrical potential [16]. Mechanical energy is lost from the oscillating device due to a mismatch in mechanical impedance [16]. Electrical energy is lost within the piezoelectric material converting a mechanical strain into an electrical potential [16].

Rayleigh damping is a common method utilized to incorporate both the mass and stiffness material properties when analyzing a structure in a dynamic environment [17]. This method begins with damping in the usual form

$$f(t) = m\frac{d^2u}{dt^2} + c\frac{du}{dt} + ku,\tag{8}$$

where $f(t)$ is the force as a function of time (t), m is the mass, u is the displacement, c is the damping parameter, and k is system stiffness [17]. Rayleigh damping uses the terms, α_{dM} and β_{dK}, to represent the damping parameter, c, in equation as a fraction of the mass and stiffness as follows

$$c = \alpha_{dM}m + \beta_{dK}k,\tag{9}$$

where α_{dM} is the mass damping parameter and β_{dK} is the stiffness damping parameter [17]. Manipulation of equation (8) and recalling that the resonant frequency, ω_0, of an undamped system is given by

$$\omega_0 = \sqrt{\frac{k}{m}},\tag{10}$$

leads to

$$\xi = \frac{1}{2}(\frac{\alpha_{dM}}{\omega_0} + \beta_{dK}\omega_0),\tag{11}$$

the Rayleigh damping parameter at resonance [17].

The contributions of the mass and stiffness damping terms are captured in Figure 19 [18]. The mass damping term, $\alpha_{dM}/2\omega_0$, indicated by the green line produces an inverse relationship between the damping ratio, ξ, and response frequency, and dominates

25

at low frequency [18]. Dominating at high frequencies is the stiffness damping term, $\beta_{dK}/2\omega_0$, indicated by the red line that produces a linear relationship between the damping ratio and response frequency [18]. The combination of the mass and stiffness damping parameters is shown in blue [18]. The μ and λ of this plot are not applicable to the harvester under test, but the shapes of the curves apply and demonstrate the affect these parameters have on the damping of the piezoelectric energy harvester.

Figure 19.   Damping Ratio vs. Frequency
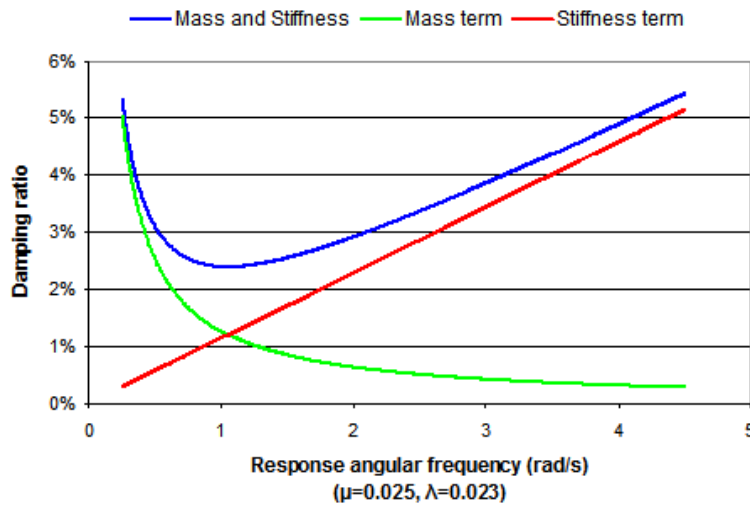
The mass damping term indicated by the green line produces an inverse relationship and dominates at low frequency. The stiffness damping term indicated by the red line produces a linear relationship and dominates at high frequency. The combination of the mass and stiffness damping terms is shown in blue. The μ and λ of this plot are not applicable to this thesis, but the shape of the curves apply and demonstrate the affect these parameters have on the damping of the piezoelectric energy harvester. Source: Rayleigh Damping: Guidance (n.d.). OracFlex. [Online]. Available: http://www.orcina.com/SoftwareProducts/OrcaFlex/Documentation/Help/Content/html/RayleighDamping,Guidance.htm. Accessed: Oct. 13, 2015

The quality factor, Q, of an oscillator describes the level of damping experienced by the system and is given by

$$Q = \frac{\omega_0}{\Delta\omega} = \frac{1}{2\xi}. \tag{12}$$

For very under-damped systems ($\xi \ll 1$), Q is related to the Rayleigh damping parameter. This relationship allows for the determination of the mass and stiffness damping

parameters, α_{dM} and β_{dK}, once the Rayleigh damping parameter, ξ, has been determined experimentally. The quality factor measured here in Chapter IV will determine the damping parameters entered into the computer models in Chapter V.

Solving equation (12), using Figures 16 and 17, yields quality factors of $Q_1 = 5.9$ at 177 Hz and $Q_2 = 44.6$ at 669 Hz. Accordingly, the overall damping factors are $\xi_1 = 8.47 * 10^{-2}$ and $\xi_2 = 1.12 * 10^{-2}$. The mass and stiffness damping parameters of the system can be determined by solving the system of equations [17] created by the two resonant peaks,

$$\xi_1 = \frac{\alpha_{dM}}{2\omega_1} + \frac{\omega_1}{2}\beta_{dK}$$

$$\xi_2 = \frac{\alpha_{dM}}{2\omega_2} + \frac{\omega_2}{2}\beta_{dK} \tag{13}$$

Equation (13) produces the values, $\alpha_{dM} = 196$ and $\beta_{dK} = -5.73 * 10^{-6}$, entered into the COMSOL solid mechanics Rayleigh damping nodes for both the linear elastic materials and the piezoelectric material.

The piezoelectric energy harvester was physically mounted on top of a brass plate with a 1 mm deep cavity. The movement of the device over this cavity may cause a pressure change and flow of the air creating an effect known as squeeze-film damping [19]. This effect can become significant to the damping analysis if the cavity is less than one tenth of the rectangular plate dimensions [20]. Because the ratio for this device and mount is 0.26, the effect is not expected to dominate the damping analysis but is included as a Thin Film boundary load under COMSOL solid mechanics physics.

G.   HIGH-SPEED IMAGING

Because of the small scale of the device, observations of the resonant modes of excitation are difficult with the naked eye. Therefore, a high-speed camera with a macro lens and imaging software was used to capture the motion of the piezoelectric energy harvester at resonance. Figure 20 is a snapshot of the imagery taken at 1000 frames per second with an exposure of 997 microseconds. At 177 Hz the center pad of the device experiences the greatest vertical motion relative to the legs, remaining flat in the

horizontal plane but oscillating vertically. At 669 Hz, the motion is very different where the center pad oscillates only slightly in the vertical direction while the bi-fold legs synchronously deflect up and down similar to diving boards. The snapshot of the high-speed camera video was taken at an elevated angle to capture the resonant mode of excitation. The elevated angle was chosen over a lateral view because it is difficult to view motion in the z-direction when recording in the same plane of the harvester.

Figure 20.   RedLake High-Speed Camera Snapshot

A snapshot of the high-speed camera video taken at an elevated angle to capture the resonant mode of excitation. The elevated angle was chosen over a lateral view because it is difficult to view motion in the z-direction when recording in the same plane of the harvester.

H.   DATA COMPARISON

Data collected by Householder [8] indicated a resonant peak of 220 μV_{rms} at 379.3 Hz as measured by the lock-in amplifier. Emen [9] reported a resonant peak of 15 mV_{rms} at 665 Hz. While the input conditions leading to these two measurements are not completely clear, it is known that Householder [8] required the use of a Stanford Research Systems SR650 Low-Noise Preamplifier to obtain visible data. Also, Emen [9] discovered a discrepancy in the mounting method of the aluminum plate to the mechanical shaker, which may have led to the plate vibrating the piezoelectric energy harvester in Householder [8] separately from the mechanical shaker. Consequently, treating the observations in Householder [8] as anomalous, especially in light of their irreproducibility, leads to a strong conclusion that the fabrication of these piezoelectric energy harvesters is consistent and a reproducible result has been found. Observations made by Emen [9] closely match the 15.1 mV_{rms} resonant peak at 669 Hz reported earlier under the same testing conditions.

V. FINITE ELEMENT MODELING

Fabricating and testing new piezoelectric energy harvesting devices is a time consuming and costly endeavor. Therefore, it is desired to have a computational model that allows for design, optimization, and performance prediction. Due to the complexity of such devices, finite element modeling and simulation is the preferred method. COMSOL Multiphysics is a versatile software and a powerful tool for this task.

A. FINITE ELEMENT MODEL CONSTRUCTION

A geometrically parameterized model was constructed matching the dimensions of the device designed by Householder [8] as shown in Figures 21 and 22. Figure 21 is an exploded three-dimensional image of the piezoelectric energy harvester showing the layer thickness of silicon (10 μm), AlN (0.493 μm), and aluminum (1.00 μm). The face along the edge of each of the long legs is connected to the substrate.

Figure 21.   Three-Dimensional View of Piezoelectric Energy Harvester
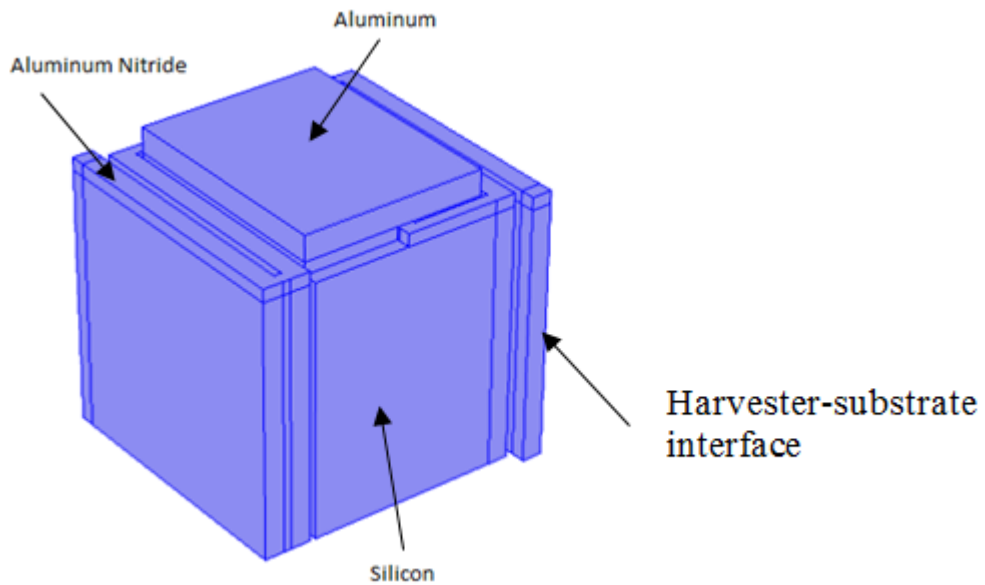
Exploded three-dimensional view of the piezoelectric energy harvester showing the layer thickness of silicon (10 μm), AlN (0.493 μm), and aluminum (1.00 μm). The face along the edge of the long legs is connected to the substrate.

Figure 22 illustrates the third generation piezoelectric energy harvester dimensions from a top-down view (xy-plane). The table below the figure includes the values entered into the finite element model.

Figure 22.   Parameterized Piezoelectric Energy Harvester
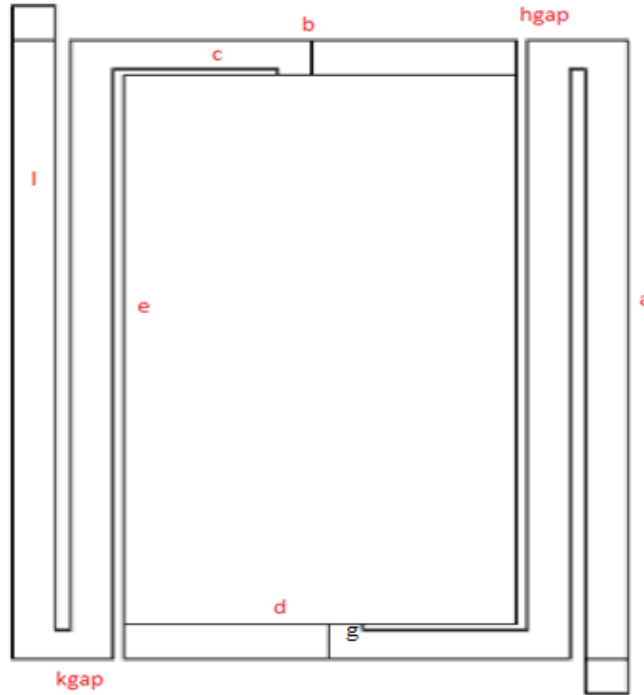
d	2300e-6[m]	pad width
e	3800e-6[m]	pad height
c	200e-6[m]	wide leg width
l	250e-6[m]	long leg width
g	40e-6[m]	pad/wide leg gap
hgap	65e-6[m]	pad/long leg gap
kgap	90e-6[m]	long leg gap
b	d+hgap	wide leg length
a	e+3*c+3*g	long leg length

Top-down view (xy-plane) of piezoelectric energy harvester, with parameters entered into the finite element model tabulated below.

Once the geometry was created, materials were assigned to the layers as follows. Silicon (from the COMSOL built-in material library) was assigned to the bottom layer, with a manually updated Young's modulus of 173.3 GPa as measured by Householder [8]. AlN (from the COMSOL piezoelectric material library) was assigned to the middle layer with a manually updated Young's modulus of 384.0 GPA as measured by Householder [8], and aluminum (from the COMSOL built-in material library) was assigned to the top layer (center pad).

COMSOL 5.1 has responded to the increased interest in piezoelectric energy harvesting and now features new piezoelectric device physics under the structural mechanics module that automatically links the previously available solid mechanics physics and electrostatics physics for ease of use. Within the solid mechanics physics, the aluminum and silicon layers were assigned as linear elastic materials and the aluminum nitride layer was assigned as the piezoelectric material. A prescribed acceleration boundary constraint was applied to the faces at the ends of the legs that are in contact with the substrate (in the zx-plane) to simulate the vibrational motion of the shaker as indicated in Figure 23. The prescribed acceleration in the x- and y-directions was set at zero, and the prescribed acceleration in the z-direction was set to 25.2 m/s^2, corresponding to the average acceleration of the shaker from characterization data found in Chapter IV. Rayleigh damping was applied to the linear elastic materials (silicon and aluminum) as well as the piezoelectric material (AlN) using the values, $\alpha_{dM} = 196$ and $\beta_{dK} = -5.73*10^{-6}$, determined in Chapter IV. Thin-film damping was added as a boundary load to the bottom surface (reference plane) of the harvester to account for squeeze-film damping as indicated in Figure 23. The dynamic viscosity of air at 300 K (1.846*10^{-6} Pa-s) was included under the fluid properties acting on the surface with a height below the reference plane set at 1 mm, corresponding to the cavity in the brass plate above which the piezoelectric energy harvester was mounted. A ground was applied as a boundary condition under electrostatics physics at the bottom right connection of the harvester to the substrate as indicated in Figure 23. A terminal was applied as a boundary condition at the upper left connection of the harvester to the substrate.

31

The electric circuit physics contained within the AC/DC module was added to the finite element model to enable output voltage predictions. A resistor, R_1, and capacitor, C_1, were added in parallel between the ground (node 0) and node 1 to simulate the input impedance of the measurement instrument, as shown in Figure 23.

Figure 23.   COMSOL Finite Element Model
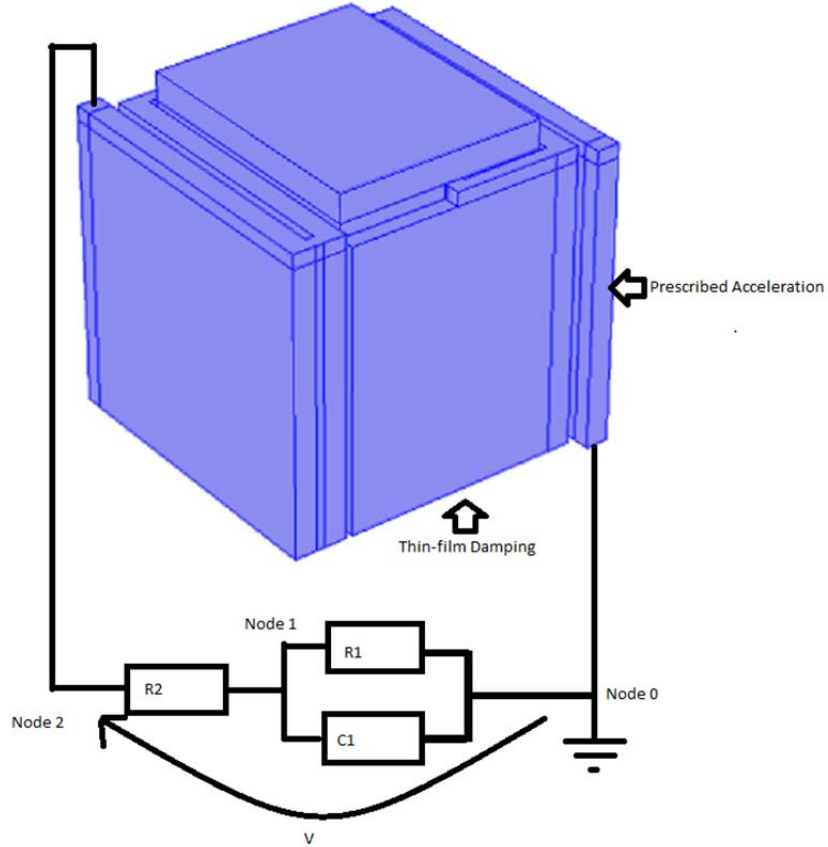
Finite element model used to predict experimental results. The prescribed acceleration arrow indicates the face along which the acceleration boundary condition was applied (note that the face along the backside of the opposite leg also received this boundary condition). The thin-film damping arrow indicates that the thin-film boundary load was applied to the bottom face of the harvester. R1 and C1 are the input resistance and capacitance of the measurement instrument. R2 is 10^{12} Ω.

To simulate measurements taken by the lock-in amplifier, the input impedance, consisting of the parallel combination of a 10 MΩ resistor (R_1) with a 15 pF capacitor (C_1), was included in the finite element model as a load to the harvester [14]. An external

I-terminal at node 2 was linked to the terminal voltage (terminal one) from the electrostatics physics to capture the output potential of the harvester. Between node one and node two an additional resistor, R_2, accounting for the conductivity of the silicon, was added to restore the measuring instrument as a high input impedance device. Initial simulations indicated an output potential significantly lower than expected. This is most likely because the doping concentration of the silicon used in the piezoelectric energy harvester is much greater than the basic silicon data found in the COMSOL material library data. To confirm this, the resistance of the model was measured for comparison with experimental data. The experimentally determined internal impedance of the piezoelectric energy harvester was measured on the order of 10^5 Ω (297 kΩ precisely), whereas the model predicted an impedance on the order of 10^{17} Ω. Hogue and Gregory [7] noted the dependence of output potential on load impedance using COMSOL time-dependent studies, and Emen [9] measured the impedance of the piezoelectric energy harvester using a Quad Core 7600 RLC vs. frequency. Emen [9] then fit the internal impedance of the harvester data to the reactance of an 828 pF capacitor. Therefore, to restore the characteristics of the lock-in amplifier as a high-input impedance measuring device, R_2 was set to 10^{12} Ω in series with the lock-in amplifier input characteristics. This allowed the COMSOL electrical circuit physics to obtain relevant results.

The mesh used in this finite element model was a free triangular mesh of normal size broken down into two swept meshes following automatically calculated sweep paths. The first swept mesh includes the silicon and aluminum nitride layers because of their similar geometries and linking faces. A distribution of 3 elements was added to the first swept mesh so that the piezoelectric layer was not one block. The second swept mesh includes only the aluminum center pad.

Two studies were added to the finite element model, a stationary study to predict eigenfrequency and a frequency domain study to predict the behavior of the output potential vs. frequency. The frequency domain study was performed between 100 and 1000 Hz in 0.5 Hz increments. This frequency sweep range matches the experimental frequency sweep performed by the lock-in amplifier in Chapter IV.

B. FINITE ELEMENT MODEL PREDICTIONS

The eigenfrequency study predicted resonance at 219, 237, 567, 697, 810 and 3325 Hz as depicted in Figure 24. The color scale represents displacement. Red indicates maximum displacement; blue indicates minimal displacement. The 219 Hz resonance shows that the center pad of the harvester is displacing significantly in the z-direction in a planar fashion (flat motion) as observed by the camera. The 237 Hz resonance indicates the center pad of the harvester is tilted in the z-direction, rotating about the x-axis. The 567 Hz resonance shows the harvester twisting about the y-axis. The 697 Hz resonance shows the multi-fold legs synchronously displacing in the z-direction. The 810 Hz resonance shows the harvester twisting in a complex direction, and the 3325 Hz resonance shows the multi-fold legs of the harvester bowing in the z-direction. The experimental data indicated resonance at 177 Hz and 669 Hz, relatively close to the theoretical 219 and 697 Hz of the 1st and 4th modes respectively. High-speed imagery reveals the exact resonance motion of the first eigenfrequency at 177 Hz and that of the fourth eigenfrequency at 669 Hz. High-speed imagery of the other eigenfrequencies, up to 1000 Hz, was captured but no deflection was observable. Only the 219 Hz, 697 Hz and 3325 Hz modes exhibit the motion of the legs in the same direction. The deflection of the device legs in torsional modes at 237, 567, and 810 Hz in opposite directions may lead to a cancellation of charge generated by the piezoelectric effect because of the opposite stress experienced by the legs, and as such no resonant peaks in output potential were observed experimentally.

Figure 24.   Piezoelectric Energy Harvester Eigenfrequencies and Excitation
Modes
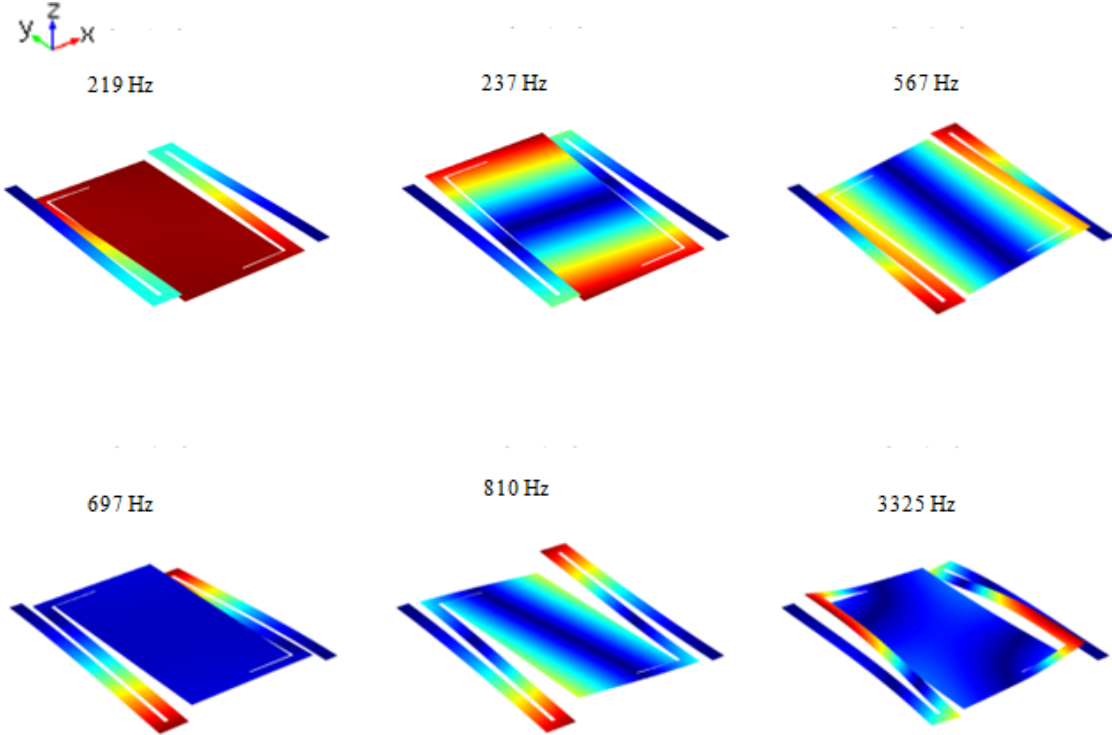
The color scale represents displacement. Red indicates maximum displacement; blue
indicates minimal displacement. The 219 Hz resonance shows that the center pad of the
harvester is displacing significantly in the z-direction in a planar fashion (flat motion).
The 237 Hz resonance indicates the center pad of the harvester is tilted in the z-direction,
rotating about the x-axis, whereas the 567 Hz resonance shows the harvester twisting
about the y-axis. The 697 Hz resonance shows the multi-fold legs synchronously
displacing in the z-direction. The 810 Hz resonance shows the harvester twisting in a
complex direction, and the 3325 Hz resonance shows the multi-fold legs of the harvester
bowing in the z-direction. Only the 219 Hz, 697 Hz and 3325 Hz modes exhibit the
motion of the legs in the same direction.

A frequency domain study in COMSOL was employed to predict the output
potential of the piezoelectric energy harvester as a function of frequency from 100 to
1000 Hz. Frequency steps were taken in 0.5 Hz increments. The model is driven by a
prescribed acceleration of 25.2 m/s^2, corresponding to the average peak acceleration
determined by the mechanical shaker during experimental testing.

The final output potential results are superimposed on the experimental data in
Figure 25 for comparison. The blue line denotes the experimental data as recorded by the

lock-in amplifier. The orange line is the COMSOL model with Rayleigh damping only, and the yellow line is the COMSOL model with both Rayleigh and squeeze-film damping. Notice the squeeze-film damping has little effect at the higher frequency as expected, due to significant leg motion and subtle center pad motion. However, the lower frequency resonant peak is reduced as a result of squeeze-film damping due to significant center pad motion, as expected.

Figure 25.   Experimental and Predicted Piezoelectric Energy Harvester Output
Potential vs. Frequency
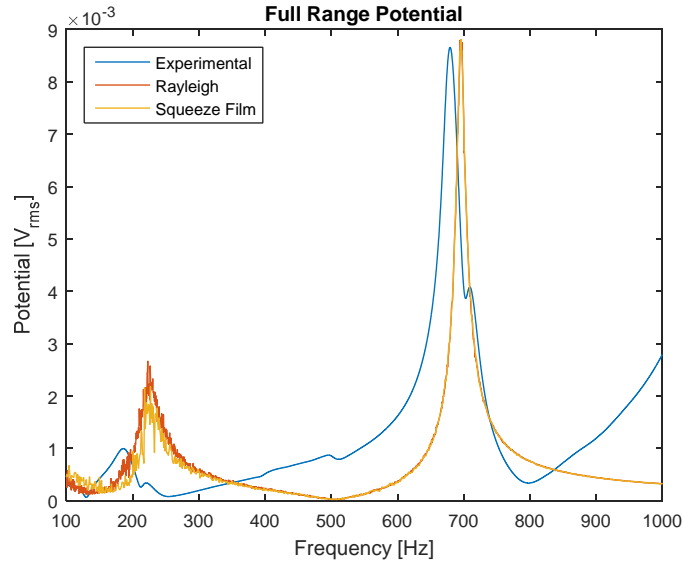
The experimental output potential from Figure 11 is plotted in blue for comparison to the finite element model prediction. The predicted output potential with only Rayleigh damping applied is plotted in orange. Further refinement to the predicted output potential with the inclusion of squeeze-film damping to the Rayleigh damping prediction is plotted in yellow. As expected the squeeze-film damping provided a significant impact at the lower frequency where the 219 Hz exication mode involved significant center pad motion. Also as expected, little impact is observed at the 697 Hz resonance because this excitation mode featured multi-fold leg motion with little center pad motion.

The peak, corresponding to the amplitude of the output potential, at the higher frequency is greater than the peak at the lower frequency because greater displacement and thus greater mechanical strain exists along the multi-fold legs at the higher frequency as evident in Figure 26 (green and black lines). The anchor point plotted in blue refers to a point where the multi-fold legs meet the substrate. The black and green lines indicate

the displacement of the ends of the multifold legs that are in sync over the entire range of frequency. The red, cyan, pink, and orange lines are the displacement of the four corners of the center pad demonstrating the planar motion of the center pad (i.e., no twisting).

Figure 26.   Predicted Piezoelectric Energy Harvester RMS Displacement vs. Frequency
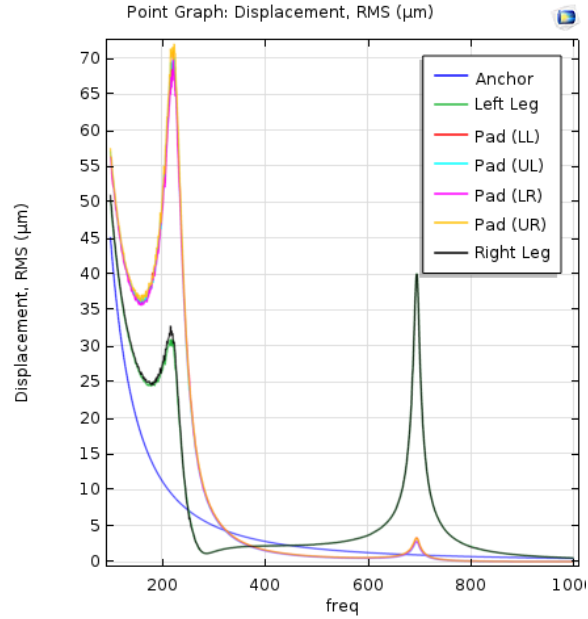

The anchor point plotted in blue refers to a point where the multi-fold legs meet the substrate. The blue line smoothly replicates the accelerometer displacement vs. frequency (displacement of the shaker itself). The red, cyan, purple, and orange lines are the displacement of the four corners of the center pad (LL-lower left, UL-upper left, LR-lower right, UR-upper right) indicating that the predicted motion of the center pad is planar with no twisting over the entire range of frequency tested. The green and black lines are the displacement of the ends of the multi-fold legs, and the model prediction shows their motion is synchronous over the entire range of frequency tested. Comparing the difference in the displacement of the black/green lines to the blue anchor line illustrates that the greatest relative displacement of the multi-fold legs leads to the greatest output potential.

The greater peak in the multi-fold leg displacement at 697 Hz matches the greatest output potential. This proves that the fourth mode of excitation is the dominant mode for design purposes as the multi-fold legs experience the greatest strain, and accordingly the greatest piezoelectric output potential. Comparing the difference in the displacement of the black/green lines to the blue anchor line illustrates that the greatest

relative displacement of the multi-fold legs leads to proportionally greater strain and greatest output potential as shown in Figure 27.

Figure 27.   Relative Displacement of Multi-fold Legs vs. Frequency
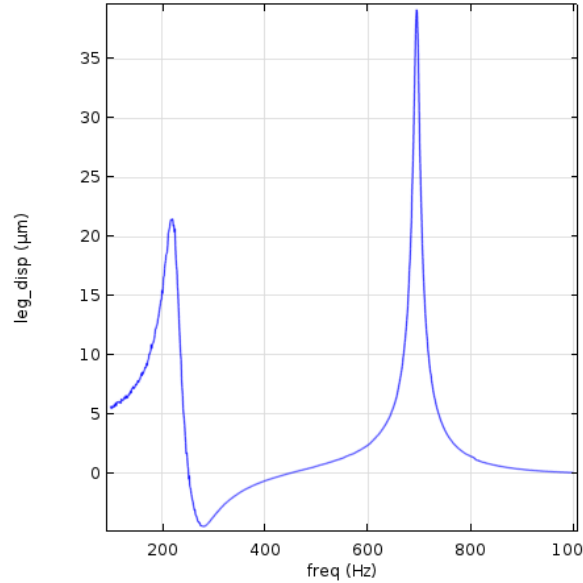
This plot demonstrates that the greatest relative displacement between the anchor point and the ends of the multi-fold legs leads to proportionally greater strain and thus greater output potential. This also demonstrates the importance of the multi-fold legs moving in sync and that the fourth resonant mode is the dominate mode in terms of output potential.

The COMSOL finite element model predicted output potential appears to match the experimental data reasonably well with a noticeable frequency shift and slightly higher potential peak at the lower resonant frequency. It is left to future work to investigate these differences and refine the model.

VI. SUMMARY

A. CONCLUSIONS

The Naval Postgraduate School has an ongoing project to develop a piezoelectric energy harvesting MEMS device that will resonant at 60 Hz, and is capable of deployment aboard naval shipping, and ground and air assault transportation. A promising device has been designed by Gregory [7] and Householder [8]. The design utilizes multi-fold legs and a center pad mass to reduce the resonant frequency toward the range of machinery vibrations [7]. Several of these devices were fabricated by MEMSCap under their PiezoMUMPS line and tested, demonstrating the capability to recapture wasted vibrational energy and convert it to usable electrical power. Consistent and reproducible experimental results are reported in this thesis and by Emen [9]. The piezoelectric energy harvester produced a maximum output voltage of 15.1 mV$_{rms}$ at 669 Hz, corresponding to the fourth mode of excitation where multi-fold leg displacement is greatest.

A finite element model was created in COMSOL Multiphysics incorporating experimentally measured material properties. Rayleigh damping was used to connect experimentally determined quality factors to modeling software damping parameters. The mass damping parameter, $\alpha_{dM} = 196 s^{-1}$, and the stiffness damping parameter, $\beta_{dK} = -5.73 * 10^{-6} s$, was included in the model along with the effects of squeeze-film damping. The finite element model provides a good prediction of the output potential of a given piezoelectric energy harvesting device vs. frequency, and can be used to optimize the design to reach the project goal.

B. FUTURE WORK

The model developed for this thesis performs well at predicting the experimentally obtained data, but its prediction of resonant frequency is slightly higher in both resonant modes. The resonant peaks also predict a higher output potential than measured despite incorporating the damping conditions. Continued damping analysis and

perhaps the inclusion of comb-drive Couette flow or Hagen-Poiseulle flow in [19] are of interest. The effects of dielectric losses and other losses also warrant investigation. Furthermore, the intrinsic stress within the piezoelectric energy harvester may lead to variations in both the resonant frequency of the device and its corresponding output potential, and merits attention and inclusion within the finite element model. The goal of the project remains to develop a device that resonates at 60 Hz. Therefore, modifications of materials, layer thicknesses, or geometry can be used to optimize the device to reach the goal. Fabrication in the NPS cleanroom still requires perfecting the microfabrication steps and processes initiated by Gregory [7] to build the optimized device. The third generation piezoelectric device was tested under various conditions for over 11 hours, and durability is important to the implementation of these devices. A fatigue analysis and a thermodynamic analysis would contribute significantly toward understanding how these devices could be deployed aboard naval shipping, and ground and air assault vehicles.

APPENDIX

Table 1.   Lock-In Amplifier Settings

Ref Phase	Gain / TC	Trace Scan	Aux Outputs
As desired	Sensitivity: As needed to prevent clipping	Store:	Aux Output: 1
Harmonic #1	Reserve: Manual	• 1 R (V_{rms})	Fixed
	Man Reserve: Value Automatic	• 2 F (freq.)	Voltage: 0.000V
	Time Constant: 100 ms	• 3 θ (phase)	Trigger: No
	Filter dB/oct: 24	Sample Rate: 512 Hz	
	Synchronous: Off	Scan Length: 31.250s	
		1 shot	
Input Filters	Output Offset	Display Scale	Math
Source: A	CH 1	As desired	Not used
Grounding: Ground	Source: R		
Coupling: AC	Offset & Expand		
Line Notches: Both	• X		
	• Offset: 0.00%		
	• Expand: 1		

Table 2.   Signal Conditioner Settings

Full Scale Range [g]	10
Mode Switch	Op
Filter	In
Input Lo	Gnd
Lo Freq	< .1 Hz
Sensitivity Set [pC/g]	1.00
• Multiplier	10

Table 3.   Imaging Software Settings

Sensor Gain [dB]	-3		Exposure Mode	Single
Exposure [µs]	997		Dynamic Range	8 bit
Rate [fps]	1000		Binning	1X1
Gamma	1		Pixel Depth	8 bit

THIS PAGE INTENTIONALLY LEFT BLANK

LIST OF REFERENCES

[1]   Executive Office of the President, The president's climate action plan. The White House, Washington, DC, June 2013. [Online]. Available: https://www.whitehouse.gov/sites/default/files/image/president27sclimateactionplan.pdf. Accessed: Oct. 15, 2005.

[2]   Deputy Secretary of Defense, Deputy's management action group guidance for a comprehensive defense energy policy. Department of Defense, Washington, DC, June 2013. [Online]. Available: http://energy.defense.gov/Portals/25/Documents/Blog/20130708_DMAG_Energy_Memo.pdf. Accessed: Oct. 15, 2015.

[3]   Deputy Commandant for Combat Development and Integration, 2012 U.S. Marine Corps S&T strategic plan. United States Marine Corps, Washington, DC, January 2012. [Online]. Available: http://www.onr.navy.mil/~/media/Files/About-ONR/USMC-ST-Strat-Plan-2012-Final-31Jan.ashx. Accessed: Oct. 15, 2005.

[4]   National Electrical Manufacturers Association, Energy efficiency & economic growth. Rosslyn, VA, 2011. Available: https://www.nema.org/Policy/Documents/Energy-Efficiency-and-Economic-Growth-4web.pdf. Accessed: Oct. 15, 2015.

[5]   R. Das. (2013). Piezoelectric energy harvesting 2013–2023: Forecasts, technologies, players. [Online]. Available: http://www.idtechex.com/research/reports/piezoelectric-energy-harvesting-2013-2023-forecasts-technologies-players-000320.asp. Accessed: Oct. 15, 2015.

[6]   H. A. Sodano et al. "Comparison of piezoelectric energy harvesting devices for recharging batteries," *J.of Intell. Material Syst. and Structures*, vol. 16, pp. 799–807, Oct. 2005.

[7]   D. B. Hogue and S. M. Gregory, "MEMS-based waste vibrational energy harvesters," M.S. thesis, Dept. Physics, Naval Postgraduate School, Monterey, CA, 2013.

[8]   T. J. Householder, "MEMS-based waste vibration and acoustic energy harvesters," M.S. thesis, Dept. Physics, Naval Postgraduate School, Monterey, CA, 2014.

[9]   S. Emen, "Power conditioning for MEMS-based waste vibrational energy harvester," M.S. thesis, Dept. Physics, Naval Postgraduate School, Monterey, CA, 2015.

[10]   C. Liu, *Foundations of MEMS*, 2nd ed. Upper Saddle River, NJ: Prentice Hall, 2012.

[11]   T. Hehn and Y. Manoli, *CMOS Circuits for Piezoelectric Energy Harvesters*. Dordrecht, Netherlands: Springer Netherlands, 2015, pp. 21–39.

[12]   D. C. Baughman, "Creation and optimization of novel solar cell power via bimetal piezoelectric MEMS device," M.S. thesis, Dept. Physics, Naval Postgraduate School, Monterey, CA, 2011.

[13]   *Instruction Manual Dual-Mode Model 114 Amplifier*, Acoustic Power Systems Inc., Carlsbad, CA, 1984, pp. 5–7.

[14]   *Model SR850 DSP Lock-In Amplifier*, Rev. 1.3, Stanford Research Systems, Sunnyvale, CA, 1992, 3.1-3.3.

[15]   *Model 2775A Signal Conditioner Instruction Manual*, Rev. BB, Endevco, San Juan Capistrano, CA, 2005, 3.4–3.7.

[16]   S. Kim et al. "Piezoelectric MEMS for Energy Harvesting," *MRS Bulletin*, vol. 37, pp. 1039–1050, Nov 2012.

[17]   Multiphysics Cyclopedia Help Feature. (2015, April). Damping sources, about damping, and Rayleigh damping. *COMSOL Multiphysics Version 5.1*. Accessed Oct 13, 2015.

[18]   Rayleigh Damping: Guidance (n.d.). OracFlex. [Online]. Available: http://www.orcina.com/SoftwareProducts/OrcaFlex/Documentation/Help/Content/html/RayleighDamping,Guidance.htm. Accessed: Oct. 13, 2015.

[19]   T. Klose et al. "Fluidmechanical damping analysis of resonant micromirrors with out-of-plane comb drive," in *Proc. COMSOL Conf.*, Hannover, 2008, [Online]. Available: http://www.comsol.com/paper/download/37065/Klose.pdf. Accessed: Oct. 27, 2015.

[20]   M. Bao and Y. Yang, "Squeeze film air damping in MEMS," *Sensors and Actuators A*, vol. 136, pp. 3–27, May 2007.

INITIAL DISTRIBUTION LIST

1.   Defense Technical Information Center
      Ft. Belvoir, Virginia

2.   Dudley Knox Library
      Naval Postgraduate School
      Monterey, California